Accepted Manuscript

High-pressure high-temperature stability of *hcp*-Ir_xOs_{1-x} (x = 0.50 and 0.55) alloys

Kirill V. Yusenko, Elena Bykova, Maxim Bykov, Sergey A. Gromilov, Alexander V. Kurnosov, Clemens Prescher, Vitali B. Prakapenka, Wilson A. Crichton, Michael Hanfland, Serena Margadonna, Leonid S. Dubrovinsky

PII: S0925-8388(16)34127-5

DOI: 10.1016/j.jallcom.2016.12.207

Reference: JALCOM 40129

To appear in: *Journal of Alloys and Compounds*

Received Date: 19 September 2016

Revised Date: 10 December 2016

Accepted Date: 16 December 2016

Please cite this article as: K.V. Yusenko, E. Bykova, M. Bykov, S.A. Gromilov, A.V. Kurnosov, C. Prescher, V.B. Prakapenka, W.A. Crichton, M. Hanfland, S. Margadonna, L.S. Dubrovinsky, High-pressure high-temperature stability of *hcp*-Ir_xOs_{1-x} (x = 0.50 and 0.55) alloys, *Journal of Alloys and Compounds* (2017), doi: 10.1016/j.jallcom.2016.12.207.

Kirill V. Yusenko[1,*], Elena Bykova[2,3], Maxim Bykov[3,4], Sergey A. Gromilov[5,6], Alexander V. Kurnosov[3], Clemens Prescher[7], Vitali B. Prakapenka[7], Wilson A. Crichton[8], Michael Hanfland[8], Serena Margadonna[1], and Leonid S. Dubrovinsky[3]

[1]College of Engineering, Swansea University, Bay Campus SA1 8EN, UK

[2]Materialphysik und Technologie, Lehrstuhl für Kristallographie, Physikalisches Institut, Universität Bayreuth, D-95440 Bayreuth, Germany

[3]Bayerisches Geoinstitut, Universität Bayreuth, D-95440 Bayreuth, Germany

[4]Laboratory of Crystallography, University of Bayreuth, D-95440 Bayreuth, Germany

[5]Department of Physics, Novosibirsk State University, Pirogova str. 2, 630090 Novosibirsk, Russia

[6]Department of Crystal Chemistry, Nikolaev Institute of Inorganic Chemistry, Lavrentiev ave. 3, 630090 Novosibirsk, Russia

[7]Center for Advanced Radiation Sources, University of Chicago, Chicago, Illinois 60637, USA

[8]European Synchrotron Radiation Facility, Polygone Scientifique Louis Neel, 6 rue Jules Horowitz, 38000, Grenoble, France

k.yusenko@swansea.ac.uk

Hcp-$Ir_{0.55}Os_{0.45}$ and *hcp*-$Ir_{0.50}Os_{0.50}$ alloys were synthesised by thermal decomposition of single-source precursors in hydrogen atmosphere. Both alloys correspond to a miscibility gap in the Ir─Os binary phase diagram and therefore are metastable at ambient conditions. An *in situ* powder X-ray diffraction has been used for a monitoring a formation of *hcp*-$Ir_{0.55}Os_{0.45}$ alloy from $(NH_4)_2[Ir_{0.55}Os_{0.45}Cl_6]$ precursor. A crystalline intermediate compound and nanodimentional metallic particles with a large concentration of defects has been found as key intermediates in the thermal decomposition process in hydrogen flow. High-temperature stability of titled *hcp*-structured alloys has been investigated upon compression up to 11 GPa using a multi-anvil press and up to 80 GPa using laser-heated diamond-anvil cells to obtain a phase separation into *fcc+hcp* mixture. Compressibility curves at room temperature as well as thermal expansion at ambient pressure and under compression up to 80 GPa were collected to obtain thermal expansion coefficients and bulk moduli. *hcp*-$Ir_{0.55}Os_{0.45}$ alloy shows bulk moduli B_0=395 GPa. Thermal expansion coefficients were estimated as $\alpha = 1.6 \cdot 10^{-5}$ K^{-1} at ambient pressure and $\alpha = 0.3 \cdot 10^{-5}$ K^{-1} at 80 GPa. Obtained high-pressure high-temperature data allowed us to construct the first model for pressure-dependent Ir─Os phase diagram.

Keywords: high-pressure, high-temperature, alloys, iridium, osmium

and extremely high melting points and densities. Due to high mechanical stability and chemical inertness, the PGMs and their alloys are widely exploited as constructional materials in the applications involving extreme conditions including high temperatures (HT), high pressures (HP) or chemical corrosion.

High-pressure phase stabilities and compressibilities of the pure PGMs were investigated up to 70-75 GPa for Rh, Ru, Ir and Pd and up to 550 and 770 GPa for Pt and Os, respectively [1-3]. For all PGMs except Ir no structural transformations were reported. Cerenius *et al.* [4] observed a formation of 14-layered superstructure in Ir above ~ 59 GPa, which was later questioned by theoretical calculations [5].

Up to now, only few PGM-based alloys such as *hcp*-$Ir_{0.70}Re_{0.30}$, *hcp*-$Rh_{0.50}Re_{0.50}$ and *hcp*-Ir_xOs_{1-x} (x = 0.20, 0.40, 0.55) were experimentally studied at high-pressure high-temperature. Each investigated binary system contains one component with hexagonal closed packed (*hcp*) structure (Ir or Rh) and another one with face centred cubic (*fcc*) structure (Re or Os). Since the components exhibit limited solubility in each other, the corresponding phase diagrams contain two solid solubility regions based on *hcp*-/*fcc*-structure and a miscibility gap in between. It is however possible to synthesize metastable solid solutions with compositions corresponding to a miscibility gap region using thermal decomposition of the single-phase bimetallic precursors [6-8].

To experimentally prove the tendency, *hcp*-$Ir_{0.7}Re_{0.3}$ and *fcc*-$Rh_{0.5}Re_{0.5}$ alloys were investigated *ex situ* under moderate pressures and temperatures (1-2 GPa and 2500 K) [6-8]. High experimental errors and small pressure response did not allow us to prove pressure dependence of phase stability in systems investigated.

Ir─Os system has been chosen due to its significance for the genesis of the natural Ir─Os─Ru and other PGM-based metallic minerals, which show complex nature and non-equilibrium character at ambient conditions. Nevertheless, only natural multi-component samples were investigated so far to clarify a situation with a mineral formation under high-pressure from the poly-component melt in Earth mantle [9-11]. Detailed investigation of synthetic samples with prespecified composition under high-temperature high-pressure up to their melting point may allow us to understand details of minerals formation and occurrence.

Recently high-pressure behaviour of *hcp*-Ir_xOs_{1-x} (x = 0.20, 0.40, 0.55) alloys was studied up to 20-30 GPa at room temperature [12]. It has been shown that, the composition dependence of bulk moduli B_0 of an alloy with molar fracture of Ir, x_{Ir}, can be expressed by the following equation:

$$B_0(x_{Ir}) = B_{Os}\left[\frac{1+x_{Ir}(\frac{V_{Ir}}{V_{Os}}-1)}{1+x_{Ir}(\frac{B_{Os}V_{Ir}}{B_{Ir}V_{Os}}-1)}\right] \quad (1),$$

Powder X-ray diffraction (PXRD) of *fcc*-$Ir_{0.80}Os_{0.20}$ recorded under compression at room temperature of the alloy up to 60 GPa reveals a kink in the compressibility curve above 20-25 GPa. The nature of such change is unclear, but it might be associated with an isostructural electronic topological transition, which occurs in pure Os [13]. However, compressibility and phase stability of various PGM-based alloys may allow us in the future to prove presumptions about electronic states of pure metals and their alloys. Experimental data collected at higher pressure and more detailed study of specialities in compressibility curves should clarify the nature of topological electronic transition in metals under high pressure.

To support our previous investigations of room-temperature compressibility for Ir─Os binary alloys and give experimental information on a high-pressure high-temperature stability of *hcp*-structured Ir─Os binary alloys, in the present study we report thermal expansion behaviour of $Ir_{0.55}Os_{0.45}$ and $Ir_{0.50}Os_{0.50}$ with *hcp*-structures at pressures up to 80 GPa and temperatures up to 3000 K. A formation of metastable *hcp*-$Ir_{0.55}Os_{0.45}$ from a single-source bimetallic precursor $(NH_4)_2[Ir_{0.55}Os_{0.45}Cl_6]$ upon heating in hydrogen atmosphere has been investigated using *in situ* powder X-ray diffraction.

2. Experimental details

[14, 15]. $(NH_4)_2[Ir_xOs_{1-x}Cl_6]$ were crystallized after adding an excess of saturated at room temperature NH_4Cl water solution to a mixture of concentrated water solutions of $K_2[OsCl_6]$ and $(NH_4)_2[IrCl_6]$. Both Ir_xOs_{1-x} samples were prepared by a thermal decomposition of $(NH_4)_2[Ir_xOs_{1-x}Cl_6]$ in 10-vol.%-H_2/90-vol.%-N_2 stream during 0.5 h at 873 K and further 10 h cooling to room temperature. Further details on synthesis and analytical characterisation of Ir_xOs_{1-x} (x = 0.50, 0.55) alloy samples are given in our previous paper [12].

Thermal gravimetric (TG) curves were measured on powders in corundum crucibles using a Stanton Redcroft TG–DSC (7-10 mg, 5 K/min, from room temperature to 1000 K) under 5 vol.% H_2/N_2 flow (20 ml/min).

Thermal decomposition of $(NH_4)_2[Ir_{0.55}Os_{0.45}Cl_6]$ has been investigated *in situ* using powder X-ray diffraction set-up on the Swiss-Norwegian Beam Lines (BM01A), ESRF. Sample, in a powder form, was placed in 0.5 mm fused quartz mark tube (Hilgenberg GmbH, Germany). Tube was connected to a 2 vol.% H_2/He flow (0.1-0.5 ml/min), and heated with a hot air stream from room temperature to 1000 K with a ramp rate of 10 K/min. Temperature has been calibrated using thermal expansion of the cell parameters for silver powder as an external standard. The wavelength (λ = 0.68894 Å) and sample-to-detector distance have been calibrated using a LaB_6 powder (NIST SRM 660c) as an external standard. Data have been collected every 20 s (approximately every 3 K

[16]. Temperature dependent PXRD patterns were plotted and analysed using Powder3D software [17]. Phase composition has been verified using the PDF database [18]. For data analysis, high-temperature PXRD data upon heating have been divided into 3 intervals (Figure 1b): below 500-550 K (pure $(NH_4)_2[Ir_{0.55}Os_{0.45}Cl_6]$ precursor); 500-750 K ($(NH_4)_2[Ir_{0.55}Os_{0.45}Cl_6]$ precursor, crystalline intermediate phases, and *hcp*-structured alloy); above 700-750 K (pure *hcp*-$Ir_{0.55}Os_{0.45}$). Detailed crystal structure of the intermediate phase has not been obtained. Nevertheless, intermediate shows diffractions patterns similar to cubic $(NH_4)_2[Ir_{0.55}Os_{0.45}Cl_6]$ precursor with slightly bigger cell parameters. Selected PXRD patterns are summarized in Figure 1c. Parametric sequential refinements were performed using TOPAS software [19]. Profile parameters for the Lorentzian function, cell parameters, and phase fractions were refined simultaneously for all phases using Rietveld refinement procedure.

High-pressure high-temperature behaviour of *hcp*-Ir_xOs_{1-x} alloys was studied using synchrotron-based powder X-ray diffraction in diamond anvil cells (DACs) as well as in multi-anvil apparatus. BX90 type DACs [20] equipped with brilliant-cut diamond anvils (120 or 250 μm culet sizes) were used for pressure generation. A sample was loaded in a hole drilled in the pre-indented rhenium gasket. Pressure was determined using equation of state of gold [21] placed in the pressure chamber as small piece of wire of 5 μm diameter and

system installed in Bayerisches Geoinstitut [22].

High-pressure PXRD data for *hcp*-$Ir_{0.50}Os_{0.50}$ were collected up to 10 GPa at room temperature at the ID09A beam-line, ESRF, (λ = 0.4145 Å, MAR 555 flat panel detector, beam size 15(v)×10(h) μm^2). The diffraction images were recorded under continuous ω-rotation of the DAC from -3 to +3° with the acquisition time of 1 s. Compressed sample was heated up to 2300 K using the external double-sided laser heating system [23]. During the heating, pressure increased up to 26.5 GPa, which was taken as a final pressure of the experiment. Room temperature PXRD data of the quenched sample were collected in the same manner as was described above.

High-pressure PXRD data for *hcp*-$Ir_{0.55}Os_{0.45}$ were collected up to 80 GPa at the 13-IDD beam-line at the APS (λ = 0.3100 Å, CCD MAR 165 detector, beam size 2(v)×3.5(h) μm^2). Diffraction images were collected without DAC rotation with the exposure time of 5 s. The sample compressed to 80 GPa was laser-heated from both sides using a pair of 1.064 μm Yb fiber lasers (beam size 3×3 μm^2) [24]. Two heating cycles were performed, in the each cycle the temperature was gradually increased up to 3000 K and then the sample was quenched; the diffraction images were measured concurrently.

Large-volume press data for *hcp*-$Ir_{0.55}Os_{0.45}$ were recorded at the beam-line ID06-LVP, ESRF, using a linear pixelated GOS detector, running sequential

distance. The detector-beam normal plane was mechanically corrected for tilt and rotation and the detector position for zero-offset and calibrated against SRM660a, at monochromatic wavelengths of 0.2296 Å, selected from the emission of a U18 undulator (6.1-6.2 mm gap) by a Cinel Si(111) double-crystal monochromator. Data for refinement were collected using a Tl:NaI scintillator counter, with a 0.2 mm pinhole and receiving slits at intermediate distance, which acted as collimators of background scattering coming from the cell assembly. The effective radius of the pseudo-rotation detector arm is 1350 mm. Collimated beam sizes were 0.5 mm horizontal by 1 mm, or the vertical anvil gap, if smaller. The *hcp*-$Ir_{0.55}Os_{0.45}$ alloy sample was finely ground with a *h*-BN powder (1:1 volume ratio) in a agate mortar and loaded into a *h*-BN (Goodfellow) capsule, before being included into the 10/4 windowed Cr:MgO assembly. Pressure was generated using the 2000 tons MAVO press in 6/8(x32) mode with carbide anvils [25]. Pressures were estimated using the equation of state of h-BN [26, 27], temperatures were estimated using the equation of state of MgO [28, 29]. Sample has been compressed up to 11.2 GPa and heated up to 3100 K under a constant pressure. Compressibility, heating, cooling and decompression curves were collected.

For data analysis, two-dimensional images were first integrated to one-dimensional intensities as a function of diffraction angle using the FIT2D

refinement implemented in JANA2006 software [31]. Compressibility curves were fitted using EoS-Fit 5.2 software [32].

3. Results

3.1. Thermal decomposition of $(NH_4)_2[Ir_{0.55}Os_{045}Cl_6]$ precursor

Thermal decomposition of $(NH_4)_2[Ir_{0.55}Os_{0.45}Cl_6]$ salt has been investigated in hydrogen atmosphere by TG (Figure 1a) and monitored *in situ* using PXRD. Temperature depended PXRD profiles are summarized in Figures 1b and 1c. Upon heating, $(NH_4)_2[Ir_{0.55}Os_{0.45}Cl_6]$ precursor does not show any phase transitions below decomposition temperature (500 K). Temperature expansion of cell parameters in the form $\alpha(T) = \alpha_0 + \alpha_1 T$ was fitted using following exponential approximation:

$$a(T) = a_0 exp\left[\int_{T_0}^{T} \alpha(T) dT\right] \qquad (2)$$

where a_0 is cell parameter at reference temperature (T_0 = 293 K) [33]. Corresponding parameters for $(NH_4)_2[Ir_{0.55}Os_{0.45}Cl_6]$ were fitted as a_0 = 9.8838(3) Å (T_0 = 293 K); $\alpha_0 = 5.4(1)\cdot 10^{-5}$ K^{-1} and $\alpha_1 = 1(1)\cdot 10^{-9}$ K^{-2} (Figure 1a, insert).

According to TG, thermal decomposition starts at 500 K with a small mass loss (1-2 mass. %). Further fast decomposition with the main mass loss occurs in

crystalline intermediate phase. Complete decomposition with a formation of single-phase *hcp*-structured alloy occurs below 650 K. Phase fractions obtained from Rietveld refinement for all phases detected during the decomposition temperature range of $(NH_4)_2[Ir_{0.55}Os_{0.45}Cl_6]$ are shown in Figure 1d. Upon heating, three overlapped steps were detected: i) simultaneous formation of intermediate and metallic phases; ii) further decomposition of precursor and intermediate; iii) growth and annealing of metallic particles.

The diffraction patterns of the metallic phase below 600 K (on heating) show diffuse, broad lines, where intensity and position can be only roughly estimated using a Rietveld approach. In these cases, it is possible that the metallic phases are more aptly described as amorphous nanoclusters rather than true nanocrystals. As a result, conventional Rietveld refinements, using only Bragg's law and isotropic Scherrer broadening effects, fail to give reasonable estimations for cell parameters and crystallites sizes below 600 K, and thermal expansion for the metallic alloys cannot be described accurately below 600 K upon heating.

The thermal decomposition of the $(NH_4)_2[Ir_{0.55}Os_{0.45}Cl_6]$ precursor leads to the formation of a metastable *hcp*-$Ir_{0.55}Os_{0.45}$ phase, which cannot be explained by the presence of any intermediate metallic phases. A smaller crystal size likely

structured gold nanocrystals [34]. As has been shown in our previous work [12], further annealing of the *hcp*-$Ir_{0.55}Os_{0.45}$ results in the decomposition the alloy onto *hcp+fcc* mixture after several days.

3.2. Thermal expansion of *hcp*-$Ir_{0.55}Os_{0.45}$ alloy at ambient pressure.

Figure 2 shows the dependence of the atomic volumes on temperature for *hcp*-$Ir_{0.55}Os_{0.45}$ alloy collected on heating from 750 to 1000 K and on cooling from 1000 K to 400 K. Thermal expansion curves obtained on heating and cooling runs demonstrate fair agreement between each other.

Corresponding volumetric thermal expansion coefficients referring to heating and cooling were fitted following analytical dependence of atomic volume on the temperature [33]. Volumetric thermal expansion coefficient in the form $\alpha(T) = \alpha_0 + \alpha_1 T$ was obtained by fitting the corresponding dataset to

$$\frac{V(T)}{Z} = \frac{V(T_0)}{Z} exp\left[\int_{T_0}^{T} \alpha(T) dT\right] \quad (3)$$

where $V(T_0)/Z$ is atomic volume at reference temperature (293 K). The resulting calculated values for α_0 and α_1 together with thermal expansion coefficients at 273 K for *hcp*-$Ir_{0.55}Os_{0.45}$ alloy and reference data for pure Ir and Os are summarized in Table 1. The volumetric thermal expansion coefficients for *hcp*-$Ir_{0.55}Os_{0.45}$ alloy are rather close to those for Os and Ir. That corresponds well

and Pt─Ru [38].

3.3. Compressibility of *hcp*-$Ir_{0.55}Os_{0.45}$ at room temperature.

Room temperature compressibility curve for *hcp*-$Ir_{0.55}Os_{0.45}$ alloy shows no pressure-induced phase transitions and can be fitted using the second-order Birch-Murnaghan equation of state (BM-EoS) which includes three parameters – V_0 (specific volume at ambient pressure), B_0 (bulk modulus), and B_0` restricted to 4 (pressure derivative of bulk modulus) (Figure 3). The data up to 52 GPa can be fitted with the same parameters as we previously reported for the compression of the same sample up to 32 GPa [12]. *fcc*-$Ir_{0.80}Os_{0.20}$ investigated earlier up to 55 GPa shows slight change in the compressibility curve above and below 20-25 GPa. On the contrary, *hcp*-$Ir_{0.55}Os_{0.45}$ does not show any change in the slope below 52 GPa. Experimental point collected at 80 GPa shows slightly smaller atomic volume in comparison with fitted data below 52 GPa, which is nevertheless in the range of experimental errors. *c*/*a* value also do not show any specialities characteristic for ETT (Figure 3, insert).

3.4. Temperature-induced transformations in *hcp*-$Ir_{0.55}Os_{0.45}$ and *hcp*-$Ir_{0.50}Os_{0.50}$ at high pressure.

temperature up to 10 GPa are shown in Figure 4. Only four experimental points were collected which are not enough to calculate reliable parameters of an equation of state. Nevertheless, bulk modulus can be roughly estimated to be of ~393 GPa using Eq. (1) and a value of atomic volume of *hcp*-$Ir_{0.50}Os_{0.50}$ at ambient conditions (14.058 $Å^3 \cdot atom^{-1}$). The 2nd order BM EoS calculated with these parameters agrees well with the experimental data (Figure 4), therefore one can use it to estimate the atomic volume of *hcp*-$Ir_{0.50}Os_{0.50}$ at higher pressures.

As synthetized *hcp*-$Ir_{0.50}Os_{0.50}$ sample shows steady diffraction rings without visible inhomogeneity and preferential orientation effects (Figure 5). The room temperature compression reveals no visible changes in a structure of diffraction rings. The laser heating at 26.5 GPa to 2300 K results in appearance of diffuse diffraction spots suggesting the recrystallization of the sample. Further analysis of the X-ray powder patterns shows the segregation into two-phase mixture: *hcp*-phase (V/Z = 13.21 $Å^3 \cdot atom^{-1}$, 81 mass.%) and *fcc*-phase (V/Z = 13.27(2) $Å^3 \cdot atom^{-1}$, 19 mass.%) (Table 4). Atomic volume of starting single-phase *hcp*-$Ir_{0.50}Os_{0.50}$ alloy (~13.24(2) $Å^3 \cdot atom^{-1}$ at 26.5 GPa) falls in between these values.

PXRD patterns of *hcp*-$Ir_{0.55}Os_{0.45}$ alloy were recorded upon heating at 11.2 GPa in the large-volume multi-anvil press (Figure 6). Decomposition of the initial *hcp*-$Ir_{0.55}Os_{0.45}$ alloy at 11.2 GPa starts at 1600 K when there appear reflections belonging to *fcc*-phase. During further temperature increase, diffraction lines of *hcp*- and *fcc*-phases become narrower, which can be associated with high-temperature recrystallization. Relative fraction of the *fcc*-phase increases with heating and reaches 75-80 mass.% at 3000 K. Annealing at 3100 K does not result in the change of relative phase fractions, which suggests equilibrium phase segregation under pressure. Final phase compositions obtained by Rietveld refinement are given in Table 4.

Pre-compressed to 80 GPa *hcp*-$Ir_{0.55}Os_{0.45}$ has been laser-heated up to 3000 K. *hcp*-$Ir_{0.55}Os_{0.45}$ phase is stable up to 2100 K. High-temperature high-pressure data can be used to estimate thermal expansion coefficient at 80 GPa which is much smaller in comparison with ambient pressure value.

Phase separation above 2100 K can be detected by appearance of new diffraction lines belonging to the *fcc*-phase (Figure 7). Below 2100 K, the diffraction rings are continuous and sample shows no inhomogeneity or preferential orientation, above this temperature there appear diffuse spots due to a recrystallization of both *fcc*- and *hcp*-phases. Thermally treated sample contains only a minor fraction of *fcc*-phase (10 mass.%). Atomic volumes of

the same trend.

4. Discussion

Crystallization of $(NH_4)_2[Ir_xOs_{1-x}Cl_6]$ salts has been performed from aqueous solutions of $K_2[OsCl_6]$ and $(NH_4)_2[IrCl_6]$. Phases with nominal composition $(NH_4)_2[Ir_xOs_{1-x}Cl_6]$ can be described as solid solutions where $[OsCl_6]^{2-}$ and $[IrCl_6]^{2-}$ occupy, on average, a single crystallographic position. The compositions of the starting aqueous solutions of $K_2[OsCl_6]$ and $(NH_4)_2[IrCl_6]$ control the composition of the resulting $(NH_4)_2[Ir_xOs_{1-x}Cl_6]$ solid phase, which makes crystallisation of $(NH_4)_2[Ir_xOs_{1-x}Cl_6]$ useful for preparation of Ir_xOs_{1-x} alloys in the whole range of concentrations [12]. All salts are single-phase and adopt a cubic crystal structure in the $Fm\bar{3}m$ space group.

Thermal decomposition of pure $(NH_4)_2[MCl_6]$ (M = Pt, Pd, Ir) in inert atmosphere (He, Ar and N_2) has been previously investigated by thermal analysis, PXRD and XAFS [38-42]. Recently, double complex salt $[Pd(NH_3)_4][PtCl_6]$ has been investigated to support the mechanism of formation of binary $Pd_{0.5}Pt_{0.5}$ alloys in inert and reductive atmosphere [43, 44]. Thermal decomposition of $(NH_4)_2[IrCl_6]$ and $(NH_4)_2[OsCl_6]$ has been investigated in details using PXRD and TG data [42]. Their TG curves in inert atmosphere do

decomposition [42]. Nevertheless, recent *in situ* study of the $(NH_4)_2[OsCl_6]$ thermal decomposition process in hydrogen atmosphere [43] suggests a formation of an amorphous intermediate $\{OsCl_4\}_x$ detected by fast EXAFS.

Previously, only platinum and palladium coordination compounds showed a formation of crystalline intermediates such as *trans*-$[Pt(NH_3)_2Cl_2]$ [44-46]. $(NH_4)_2[Ir_{0.55}Os_{0.45}Cl_6]$ salt, when heated above 500-550 K in inert or reductive atmosphere, decomposes to form a mixture of an *hcp*-structured metallic phase and an intermediate crystalline phase, which can probably be associated with the formation of Ir(III) polymeric species. Similar Ir(IV)/Ir(III) transformation has been proposed as a key step in the thermal decomposition of $[Pd(NH_3)_4][IrCl_6]$ [45].

Further *ex situ* and *in-situ* XAFS investigations of the thermal decomposition reactions similar to the study performed for $(NH_4)_2[OsCl_6]$ [43] could clarify the decomposition processes of $(NH_4)_2[Ir_xOs_{1-x}Cl_6]$ salts, and shed light on the interactions between starting compounds and intermediate phases. Additionally, such a study could give clear information about oxidation state and coordination of ions within the observed intermediate phase.

Pressure-dependent phase diagrams were constructed for the most elements of the Periodic Table. However, only few binary metallic systems were

dependent melting curves were obtained neither for pure Ir nor for Os due to their high melting points [1]. Nevertheless, a positive slope of the pressure dependent melting curve was predicted for pure Ir [46]. It seems that both metals do not show pressure or temperature induced phase transitions. Nevertheless, recently, an electronic topological transition (ETT) in 5-*d* metals has taken attention of many experimentalists and theoreticians [13, 47-50]. This transition characteristic for *hcp* metals can be attributed with peculiarities in *c*/*a* behaviour under pressure. Pure Os exhibits ETT at ~ 150 GPa which is characterized by anomaly in the unit cell parameter ratio (*c*/*a*) [47-49]. In the contrary, the same transition for pure Ir has been predicted to occur at much lower pressure around 80 GPa [50].

fcc-$Ir_{0.80}Os_{0.20}$ demonstrates a kink on the compressibility curve at around 20-25 GPa, which might be interpreted as an isostructural transition [12]. On the other hand, room temperature compression of *hcp*-Ir─Os binary alloys provokes neither phase transition nor phase separation in a whole range of pressures studied. If any ETT exists in *hcp* Os-rich alloys, it should be similar to pure osmium and occurs at higher pressure. Ir-rich *fcc* alloys, such as *fcc*-$Ir_{0.80}Os_{0.20}$, should be similar to pure Ir and even can show ETT at lower pressures in

The binary Ir─Os phase diagram has been investigated by several independent research groups [51-55] and may be considered as complete and correct. The system shows peritectic reaction *(liquid + hcp = fcc)* with a nearly vertical miscibility gap between *fcc* and *hcp* alloys (Figure 9) [51]. In general, applying a hydrostatic pressure should shift the miscibility gap towards to the phase with the larger molar volume. In the Ir─Os binary, the pressure should shift the miscibility gap toward the *fcc* region since *fcc*-alloys have slightly larger atomic volumes than *hcp*-structured alloys. Schematically, the effect of pressure on the Ir─Os binary phase diagram is demonstrated in Figure 9.

According to the phase diagram [51], *hcp*-$Ir_{0.55}Os_{0.45}$ and *hcp*-$Ir_{0.50}Os_{0.50}$ are metastable at ambient pressure. If so, two metastable *hcp*-$Ir_{0.55}Os_{0.45}$ and *hcp*-$Ir_{0.50}Os_{0.50}$ alloys form two figurative points inside the miscibility gap of the phase diagram and can be used to probe pressure dependence of the phase stability regions in the Ir─Os binary system. Corresponding phase separation after high-temperature treatment under various pressures gives an estimation of phase boundaries in case if final phase compositions and/or phase fractions are known. As an example, explained strategy has been recently applied for an investigation of the Pd─Rh binary system at ambient pressure [56].

Os. Nevertheless, direct comparison of Ir and Os response to temperature and pressure can be performed only after experimental construction of their P–T-EoS in a broad conditions range. Up to now, only thermal expansion at ambient pressure and compressibility curves at room temperature were experimentally obtained for pure Ir and Os, which builds limitations for detailed analysis of their behaviour under various high-pressure high-temperature conditions.

Compositions of two-phase samples obtained after high-temperature high-pressure treatment are summarised in Table 3 and graphically in Figure 8. Phase compositions of two-phase samples show a clear dependence of miscibility gap on the applied pressure. As expected, miscibility gap does not shift much with pressure and *hcp* boundary probably reaches 50 at.% Os above 80 GPa.

Incomplete experimental data do not allow us to construct reliable pressure dependent Ir–Os binary phase diagram. Theoretical calculations and thermodynamic modelling may help to build complete model of the diagram for further experimental improvement. The modelling might be based on the mixing parameters obtained for ambient pressure diagram, compressibility and thermal expansion curves for pure metals and their alloys as well as on the high-pressure miscibility data. Approaches for the accurate modelling of pressure dependent alloy phase diagrams are still under early development but undoubtedly only

data in the BM EoS form cannot be directly implemented into the thermodynamic modelling of phase diagrams [57]. Nevertheless, only compressibility and thermal expansion can be considered as direct information, which in general can be obtained with a high accuracy for incompressible alloys with extremely high melting points.

As miscibility gap between *fcc* and *hcp* alloys slightly depends on the temperature, the same tendency can be expected for pressure dependence. Such finding opens possibility to build a model for pressure dependent phase diagram for Ir─Os system at least in the *solidus* part and estimate dependence of the miscibility gap on the pressure based on experimental *P*─*x* and *T*─*x* particular sections and projections. Hypothetic *P*─*x* projection can be found in the supplement as an example (Figure S1).

Summary and conclusions

Metastable *hcp*-$Ir_{0.55}Os_{0.45}$ and *hcp*-$Ir_{0.50}Os_{0.50}$ alloys prepared from single source precursors can be successfully used to probe phase stability of binary phases not only under high-temperatures but also under high-pressures. As high-pressure compression of refractory alloys at room temperature does not

specimens. Thermal expansion curves obtained at ambient pressure and 80 GPa for *hcp*-$Ir_{0.55}Os_{0.45}$ can be successfully fitted with existing exponential function to obtain temperature dependent equation of state. Obtained values for thermal expansion coefficients lie between whose for pure Ir and Os. Thermal expansion coefficients coupled with compressibility parameters give us a complete pattern for high-temperature high-pressure behaviour for individual alloys and can be used to model phase stability under extreme conditions. Here we present the first experimental evidence for the pressure dependent shift of the miscibility gap in refractory alloys phase diagrams. Phase stability boundaries in the *solidus* part of the phase diagram display clear pressure dependence. Upon the compression up to 20-25 GPa, stability region of *hcp*-phase is growing, which results the shift of miscibility gap towards Ir part of the diagram. Above 25 GPa and below 80 GPa, miscibility gap does not show further change. As only limited data under compression can be obtained, detailed thermodynamic modelling should be performed to construct complete *P*─*T*─*x* diagram of the Ir─Os binary system. A construction of complete pressure-dependent phase diagram for Ir─Os binary and Ir─Os─Ru ternary systems will help to understand a formation of PGM metallic minerals in the Mantle.

The authors thank ID-09A and ID06-LVP beam-lines at the European Synchrotron Radiation Facility (ESRF) and Swiss-Norwegian beam lines (BM-01A) at the ESRF for providing us measurement time and technical support. Dr. Dmitry Chernyshov (SNBL), Dr. Vadim Dyadkin (SNBL), Fabian L.M. Bernal and Jonas Sottmann (University of Oslo) are thanked for their kind support during synchrotron-based experiments. Financial support by German Science Foundation (DFG), German Ministry of Science and Education (BMBF) is greatly appreciated. Portions of this work were performed at GeoSoilEnviroCARS (Sector 13), Advanced Photon Source (APS), Argonne National Laboratory. GeoSoilEnviroCARS is supported by the National Science Foundation - Earth Sciences (EAR-1128799) and Department of Energy-GeoSciences (DE-FG02-94ER14466). Use of the Advanced Photon Source was supported by the U. S. Department of Energy, Office of Science, Office of Basic Energy Sciences, under Contract No. DE-AC02-06CH11357. K.Y. is also grateful the EPSRC Impact Acceleration Account for the financial support.

[1] E.Y. Tonkov, E.G. Ponyatovsky, Phase transformations of elements under high pressure, CRC Press LLC, 377 p. (2005).

[2] M.I. McMahon, R.J. Nelmes, High-pressure structures and phase transformations in elemental metals Chem. Soc. Rev. 35 (2006), 943-963. DOI: 10.1039/B517777B

[3] L. Dubrovinsky, N. Dubrovinskaia, V.B. Prakapenka, A.M. Abakumov, Implementation of micro-ball nanodiamond anvils for high-pressure studies above 6 Mbar, Nat. Commun. 3(1163) (2012), 1-7. DOI: 10.1038/ncomms2160.

[4] Y. Cerenius, L. Dubrovinsky, Compressibility measurements on iridium, J. Alloys Compd, 306(1-2) (2000), 26-29. DOI: 10.1016/S0925-8388(00)00767-2

[5] S. Grussendorff, N. Chetty, H. Dreysse, Theoretical studies of iridium under pressure, J. Phys.: Condens. Matter, 15 (2003), 4127–4134.

[6] S.A. Gromilov, I.V. Korolkov, K.V. Yusenko, S.V. Korenev, T.V. D´yachkova, Y.G. Zainulin, A.P. Tyutyunnik, Phase transformations of the $Re_{0.3}Ir_{0.7}$ solid solution, J. Structur. Chem., 46 (2005), 474. DOI: 10.1007/s10947-006-0126-x

[7] S.A. Gromilov, T.V. D´yachkova, K.V. Yusenko, I.B. Kireenko, A.P. Tyutyunnik, Y.G. Zainulin, Study of the $Re_{0.50}Rh_{0.50}$ products of thermobaric treatment, J. Structur. Chem., 50 (2009), 306. DOI: 10.1007/s10947-009-0042-y.

under high-pressure and high-temperature, Int. J. Mater. Res., 104 (2013), 476. DOI: 10.3139/146.110884

[9] J.M. Bird, W.A. Bassett, Evidence of a Deep Mantle History in Terrestrial Osmium─Iridium─Ruthenium Alloys, J. Geophys. Res., 85 (1980), 5461–5470. DOI: 10.1029/JB085iB10p05461

[10] D.C. Harris, L.J. Cabri, Nomenclature of platinum-group-element alloys: review and revision, Can. Miner., 29 (1991), 231-237.

[11] R.O.C. Fonseca, V. Laurenz, G. Mallmann, A. Luguet, N. Hoehne, K.P. Jochum, New constraints on the genesis and long-term stability of Os-rich alloys in the Earth's mantle, Geochim. Cosmochim. Acta, 87 (2012), 227-242. DOI: 10.1016/j.gca.2012.04.002

[12] K.V. Yusenko, E. Bykova, M. Bykov, S.A. Gromilov, A.V. Kurnosov, C. Prescher, V.B. Prakapenka, M. Hanfland, S. van Smaalen, S. Margadonna, L.S. Dubrovinsky, Compressibility of Ir─Os alloys under high pressure, J. Alloys and Comp., 622 (2015), 155 DOI: 10.1016/j.jallcom.2014.09.210

[13] L. Dubrovinsky, N. Dubrovinskaia, E. Bykova, M. Bykov, V. Prakapenka, C. Prescher, K. Glazyrin, H.P. Liermann, M. Hanfland, M. Ekholm, Q. Feng, L.V. Pourovskii, M.I. Katsnelson, J.M. Wills, I.A. Abrikosov, The most incompressible metal osmium at static pressures above 750 gigapascals. Nature, 525(7568) (2015), 226-229 doi:10.1038/nature14681

metallic system, J. Struct. Chem., 46(6) (2005), 1052–1059. DOI: 10.1007/s10947-006-0241-8

[15] I.V. Korolkov, A.I. Gubanov, K.V. Yusenko, I.A. Baidina, S.A. Gromilov, Synthesis of non-equilibrium Pt_xOs_{1-x} solid solutions. Crystal structure of $[Pt(NH_3)_4][OsCl_6]$, J. Struct. Chem., 48(3) (2007), 486–493. DOI: 10.1007/s10947-007-0073-1

[16] V. Dyadkin, SNBL Tool-box. Grenoble, France: Swiss Norwegian Beamline at ESRF 2013.

[17] P. Rajiv, R. Dinnebier, M. Jansen, Powder 3D Parametric: A program for automated sequential and parametric Rietveld refinement using Topas, Materials Science Forum 651 (2010) 97-104.

[18] PDF-2 Release 2012 (Database), ed. S. Kabekkodu, International Centre for Diffraction Data, Newtown Square, PA, USA (2012).

[19] TOPAS v.4.0, Bruker-AXS 5465 East Cheryl Parkway – Bruker AXS – 2009

[20] I. Kantor, V. Prakapenka, A. Kantor, P. Dera, A. Kurnosov, S. Sinogeikin, N. Dubrovinskaia, and L. Dubrovinsky, BX90: A new diamond anvil cell design for X-ray diffraction and optical Measurements, Rev. Sci. Instrum., 83 (2012), 125102. http://dx.doi.org/10.1063/1.4768541

10.1073/pnas.0609013104

[22] A. Kurnosov, I. Kantor, T. Boffa-Ballaran, S. Lindhardt, L. Dubrovinsky, A. Kuznetsov, B.H. Zehnder, A novel gas-loading system for mechanically closing of various types of diamond anvil cells. Rev Sci Instrum. 2008;79:045110.

[23] I. Kupenko, L. Dubrovinsky, N. Dubrovinskaia, C. McCammon, K. Glazyrin, E. Bykova, T. Boffa Ballaran, R. Sinmyo, A.I. Chumakov, V. Potapkin, A. Kantor, R. Rüffer, M. Hanfland, W. Crichton, M. Merlini Portable double-sided laser-heating system for Mössbauer spectroscopy and X-ray diffraction experiments at synchrotron facilities with diamond anvil cells. Rev. Sci. Instruments 83(12) (2012) 124501 doi: 10.1063/1.4772458.

[24] V.B. Prakapenka, A. Kubo, A. Kuznetsov, A. Laskin, O. Shkurikhin, P. Dera, M. L. Rivers, S. R. Sutton (2008), Advanced flat top laser heating system for high pressure research at GSECARS: Application to the melting behavior of germanium, High Pressure Res., 28, 225–235, doi:10.1080/08957950802050718

[25] J. Guignard, W.A. Crichton, The large volume press facility at ID06 beamline of the European synchrotron radiation facility as a High Pressure-High Temperature deformation apparatus. Rev. Sci. Instrum. 86 (2015) 085112. DOI: http://dx.doi.org/10.1063/1.4928151

[26] Y. Le Godec, D. Martinez-Garcia, M. Mezouar, G. Syfosse, J. P. Itie, and J. M.Besson, High Press. Res. 17 (2000), 35.

boron nitride: Implications for a high-temperature pressure scale, Phys. Rev. B, 75 (2007) 224114. DOI: 10.1103/PhysRevB.75.224114

[28] L.S. Dubrovinsky, S.K. Saxena, Thermal Expansion of Periclase (MgO) and Tungsten (W) to Melting Temperatures, Phys. Chem. Minerals, 24 (1997), 547–550. DOI 10.1007/s002690050070

[29] A. Dewaele, G. Fiquet, D. Andrault□, D. Hausermann, *P—V—T* equation of state of periclase from synchrotron radiation measurements, J. Geophys. Res., 105 (2000), 2869-2877. DOI: 10.1029/1999JB900364

[30] A.P. Hammersley, S.O. Svensson, M. Hanfland, A.N. Fitch, and D. Häusermann, Two-Dimensional Detector Software: From Real Detector to Idealised Image or Two-Theta Scan, High Press. Res., 14 (1996), 235-248. DOI: 10.1080/08957959608201408

[31] V. Petříček, M. Dušek, L. Palatinus Crystallographic Computing System JANA2006: General Features. Z. Krist 229(5) (2014), 345-352 DOI 10.1515/zkri-2014-1737. http://www-xray.fzu.cz/jana/jana.html

[32] R.J. Angel, Equations of State. In Hazen, R.M., Downs, R.T. (Eds.), High-pressure, high-temperature crystal chemistry. Reviews in Mineralogy and Geochemistry, 41 (2001), 35-60. http://www.rossangel.com/

[33] R.S. Krishnan, R. Srinavasan, S. Devanarayanan (1979) Thermal expansion of crystals. Pergamon Press, Oxford

nanostructures, Nature Communications 2 (2011) 292. DOI:10.1038/ncomms1291

[35] J.W. Arblaster, Crystallographic Properties of Iridium Assessment of properties from absolute zero to the melting point, Platinum Met. Rev., 54 (2010), 93-102. DOI: 10.1595/147106710X493124

[36] J.W. Arblaster, Crystallographic Properties of Osmium Assessment of properties from absolute zero to 1300 K, Platinum Met. Rev., 57 (2013), 177-185. DOI: 10.1595/147106713X668541

[37] R.E. Edsinger, M.L. Reilly, J.F. Schooley, Thermal Expansion of Platinum And Platinum─Rhodium Alloys, J. Res. Nat. Bureau Standards 91 (1986), 333-356. http://dx.doi.org/10.6028/jres.091.037

[38] B. Barter, A.S. Darling, Thermal Expansion of Platinum─Rhodium Alloys, Platinum Met. Rev., 4 (1960), 138-140.

[39] Q. Kong, F. Baudelet, J. Han, S. Chagnot, L. Barthe, J. Headspith, R. Goldsbrough, F.E. Picca, O. Spalla Microsecond time-resolved energy-dispersive EXAFS measurement and its application to film the thermolysis of $(NH_4)_2[PtCl_6]$. Scientific Rep. 2 (2012) 1018. DOI: 10.1038/srep01018

[40] H. Rumpf, J. Hormes, A. Moller, G. Meyer, Thermal decomposition of $(NH_4)_2[PtCl_6]$ - an in situ X-ray absorption spectroscopy study. J. Synchrotron Rad. 6 (1999) 468–470. DOI:10.1107/S0909049598015994

spectroscopy. J. Synchrotron Rad. 8 (2001) 707–709. DOI:10.1107/S0909049500015958

[42] G. Meyer, A. Moller, Thermolysis of ternary ammonium chlorides of rhenium and the noble-metals. J. Less-Common Met. 170 (1991) 327–331. DOI:10.1016/0022-5088(91)90336-3

[43] T.I. Asanova, I Kantor, I.P. Asanov, S.V. Korenev, K.V. Yusenko, Thermal decomposition of ammonium hexachloroosmate. Physical Chemistry Chemical Physics (2016) DOI: 10.1039/C6CP07133C

[44] T. Asanova, I. Asanov, A. Zadesenets, E. Filatov, P. Plusnin, E. Gerasimov, S. Korenev, Study on thermal decomposition of double complex salt $[Pd(NH_3)_4][PtCl_6]$. J. Thermal. Anal. Calorim. 123 (2016) 1183–1185. DOI 10.1007/s10973-015-5002-5

[45] T.I. Asanova, I.P. Asanov, Min-Gyu Kim, E.Yu. Gerasimov, A.V. Zadesenets, P.E. Plusnin, S.V. Korenev, On formation mechanism of Pd–Ir bimetallic nanoparticles through thermal decomposition of $[Pd(NH_3)_4][IrCl_6]$. J Nanopart. Res. 15 (2013) 1994–2009. DOI 10.1007/s11051-013-1994-6

[46] G.R. Gathers, J.W. Shaner, R.S. Hixon, D.A. Young, Very high temperature thermophysical properties of solid and liquid V and Ir. High Temp. High Pressure, 11 (1979), 653.

DOI: 10.1063/1.4726203

[48] F. Occelli, D.L. Farber, J. Badro, C.M. Aracne, D.M. Teter, M. Hanfland, B. Canny, B. Couzinet, Experimental evidence for a high-pressure isostructural phase transition in osmium, Phys. Rev. Lett., 93(9) (2004), 095502. DOI: http://dx.doi.org/10.1103/PhysRevLett.93.095502

[49] T. Kenichi, Bulk modulus of osmium: High-pressure powder x-ray diffraction experiments under quasi-hydrostatic conditions, Phys. Rev. B, 70 (2004), 012101. DOI: http://dx.doi.org/10.1103/PhysRevB.70.012101

[50] A.A. Tal, M.I. Katsnelson, M. Ekholm, H.J.M.Jönsson, L. Dubrovinsky, N. Dubrovinskaia, I.A. Abrikosov, Pressure-induced crossing of the core levels in 5d metals, Phys. Rev. B, 93 (2016) 205150. DOI:https://doi.org/10.1103/PhysRevB.93.205150

[51] H. Okamoto, The Ir─Os (Iridium─Osmium) System, J. Phase Equilib., 15 (1994), 55-57. DOI: 10.1007/BF02667683

[52] R.D. Reiswig, J.M. Dickinson, The Osmium─Iridium Equilibrium Diagram, Trans. Metall. Soc. AIME, 230 (1964) 469-472.

[53] H.C. Vacher, C.J. Bechtoldt, E. Maxwell, Structure of Some Iridium─Osmium Alloys, J. Metals, 200(1) (1954), 80-82.

(1963), 182-183. DOI: http://dx.doi.org/10.1103/PhysRev.129.182

[55] R.S. Rudman, Lattice parameters of some h.c.p. binary alloys of rhenium and osmium: Re─W, Re─Ir, Re─Pt, Os─Ir, Os─Pt, J. Less-Common Metals, 12(1) (1967), 79-81. DOI: 10.1016/0022-5088(67)90075-6

[56] Y.V. Shubin, P.E. Plyusnin, S.V. Korenev, Determination of the equilibrium miscibility gap in the Pd─Rh alloy system using metal nanopowders obtained by decomposition of coordination compounds, J Alloys Compd. 622 (2015), 1055-1060. DOI: 10.1016/j.jallcom.2014.10.187

[57] Xiao-Gang Lu, M. Selleby, B. Sundman, Implementation of a new model for pressure dependence of condensed phases in Thermo-Calc, Computer Coupling of Phase Diagrams and Thermochemistry, 29 (2005), 49-55. doi:10.1016/j.calphad.2005.04.001

temperature dependence of cubic cell parameter for $(NH_4)_2[Ir_{0.55}Os_{0.45}Cl_6]$; solid line corresponds to fitted curve according to Equation 1). B: Temperature dependence of PXRD patterns corresponded to the thermal decomposition of $(NH_4)_2[Ir_{0.55}Os_{0.45}Cl_6]$ in hydrogen atmosphere (2 vol.% H_2/He flow, λ = 0.68894 Å, *2D-film top view*). C: Selected PXRD patterns obtained at various temperatures. D: weight fractions for intermediate phases upon heating of $(NH_4)_2[Ir_{0.55}Os_{0.45}Cl_6]$.

Figure 2. Temperature dependence of atomic volumes for Ir [35], Os [36], and *hcp*-$Ir_{0.55}Os_{0.45}$ alloy formed from $(NH_4)_2[Ir_{0.55}Os_{0.45}Cl_6]$ precursor (*red hexagons – heating, blue – cooling, lines correspond to fits according to Equation 2 and Table 1*).

Figure 3. Pressure dependence of the atomic volume of *hcp*-$Ir_{0.55}Os_{0.45}$ alloy at room temperature. Open circles represent experimental data, solid line is the second-order BM-EoS fitted using parameters obtained in [12] (Table 2). Insert shows pressure dependence of *c*/*a* value.

Figure 4. Evolution of *hcp*-$Ir_{0.50}Os_{0.50}$ under room-temperature compression (open symbols) and with heating under pressure (solid symbols). Heating at 25.6 GPa to 2300 K results in a two-phase mixture (*fcc*+*hcp*). Compressibility curve for *hcp*-$Ir_{0.50}Os_{0.50}$ up to 10 GPa with an extrapolation to 27 GPa. Hexagons represent *hcp*

Figure 5. Least-square fit for *hcp*-$Ir_{0.50}Os_{0.50}$ at 13.7 GPa (*left*). The same sample after heating at 2300 K under 26.7 GPa (*right*). Experimental data-points are shown as squares, refined profile – as solid line, radial sweeps of 2D images are shown in the middle, difference curves are shown at the bottom, (room temperature, λ = 0.4145 Å).

Figure 6. *In situ* PXRD data collected at the large-volume press for *hcp*-$Ir_{0.55}Os_{0.45}$ at constant pressure (11.2 GPa) with increasing temperature (λ = 0.2296 Å) and representative integrated PXRD profile at 2100 K.

Figure 7. Dependence of atomic volume on the temperature for *hcp*-$Ir_{0.55}Os_{0.45}$ at 80 GPa. Hexagons represent *hcp* phase; squares – *fcc* in two-phase region; line corresponds to the fit according to Equation 2. Points at 300 K correspond to the quenched sample.

Figure 8. Least-square fit for *hcp*-$Ir_{0.55}Os_{0.45}$ at 1370(8) (left) and 2346(8) K (right) under 80 GPa (λ = 0.3100 Å). Experimental data-points are shown as squares, refined profile – as solid line, difference curve is shown at the bottom. Inset shows radial sweep of 2D images.

Figure 9. *Left*: experimental Ir─Os binary phase diagram at ambient pressure (P_0) according to [51] (firm line) and schematic drawing of the same diagram with

representation of phase separation in *hcp*-$Ir_{0.50}Os_{0.50}$ and *hcp*-$Ir_{0.55}Os_{0.45}$ under various pressures.

hcp-Os (ambient pressure)	13.9843(2)	1.35(1)	4.7(2)	1.36	[35]
hcp-$Ir_{0.55}Os_{0.45}$ (ambient pressure, heating)	14.11(1)	1.57(3)	1.9(4)	1.6(5)	present work
hcp-$Ir_{0.55}Os_{0.45}$ (ambient pressure, cooling)	14.11(1)	1.36(6)	4.8(9)	1.4(5)	present work
hcp-$Ir_{0.55}Os_{0.45}$ (P = 80 GPa, heating)	12.25(1)	0.31(7)	0.3(4)	0.3(5)	present work
fcc-Ir (ambient pressure)	14.1475(3)	1.66(2)	7.3(3)	1.68	[36]

fcc-$Ir_{0.80}Os_{0.20}$ (20—55 GPa)	14.112(2)	13.98(2)	484(7)	[12] / ESRF in oil
hcp-$Ir_{0.55}Os_{0.45}$ (0—32 GPa)	14.092(2)	14.07(2)	393(7)	[12] / APS in Ne
hcp-$Ir_{0.55}Os_{0.45}$ (0—52 GPa)	14.092(2)	14.07(2)	395(5)	Present study/APS in Ne

[a]atomic volume refined from PXRD data at ambient conditions;

[b]atomic volume obtained from BM-EoS;

[c]B_0` = 4.

Table 3. Crystallographic data for as synthetized and anne

Composition	As synthetized (873 K, 0.5 h) [12]				Annealed				
					ambient pressure, 1273 K, 40 h [12]		11.2 GPa, 3000 K		26.5 GP
	a, Å	*c*, Å	Space group	V_0/Z, Å$^3\cdot$atom^{-1}	Phase	Composition	Phase	Composition	Phase
hcp-$Ir_{0.55}Os_{0.45}$	2.728(2)	4.373(3)	$P6_3\backslash mmc$	14.092(2)	$Fm\bar{3}m$	90 % *fcc*-$Ir_{0.75}Os_{0.25}$	$Fm\bar{3}m$	79 %	—
					$P6_3\backslash mmc$	10 % *hcp*-$Ir_{0.36}Os_{0.64}$	$P6_3\backslash mmc$	21 %	—
hcp-$Ir_{0.50}Os_{0.50}$	2.729(2)	4.361(3)	$P6_3\backslash mmc$	14.058(2)	$Fm\bar{3}m$	68 % *fcc*-$Ir_{0.75}Os_{0.25}$	—	—	$Fm\bar{3}m$
					$P6_3\backslash mmc$	32 % *hcp*-$Ir_{0.35}Os_{0.65}$	—	—	$P6_3\backslash mmc$

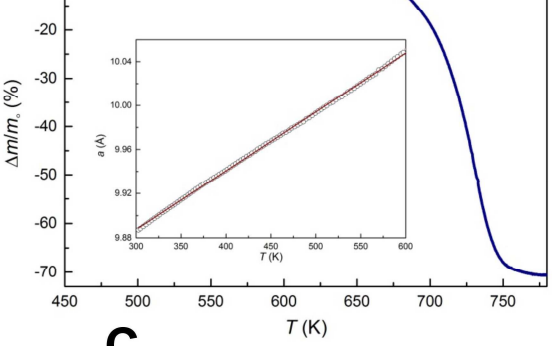
Δm/m₀ (%)
T (K)
a (Å)
T (K)

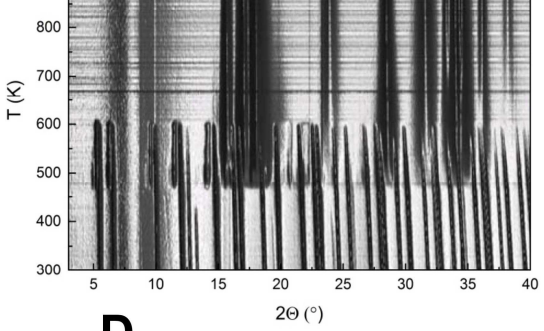
T (K)
2Θ (°)

C

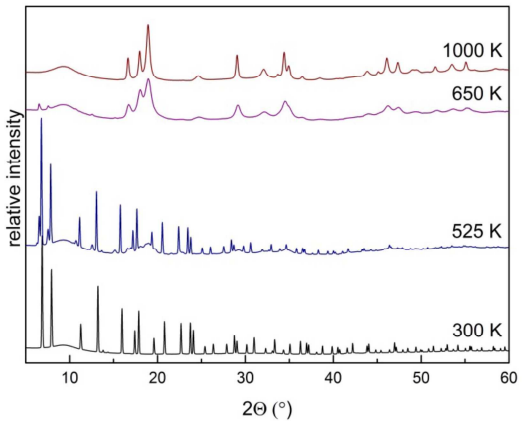
1000 K
650 K
525 K
300 K
relative intensity
2Θ (°)

D

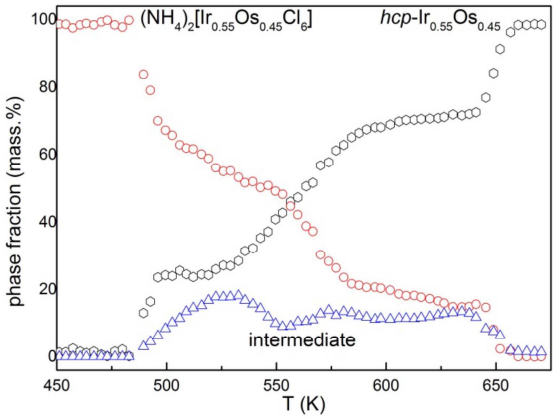
(NH4)2[Ir0.55Os0.45Cl6]
hcp-Ir0.55Os0.45
intermediate
phase fraction (mass.%)
T (K)

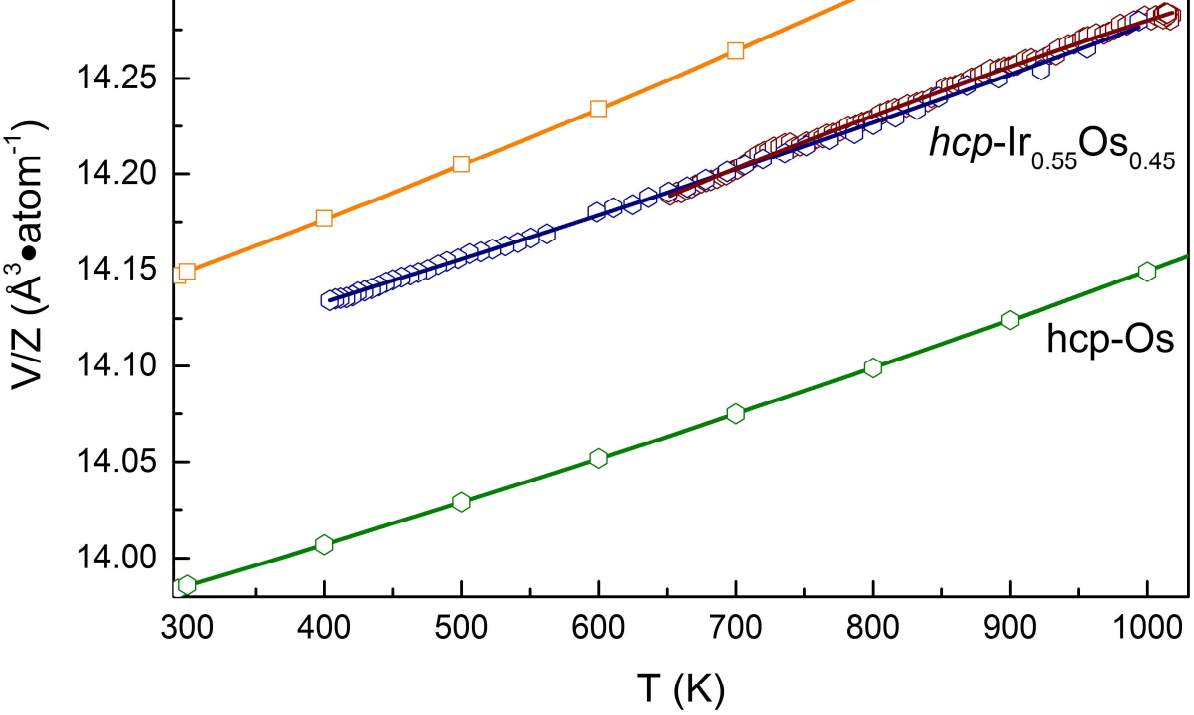
14.25
14.20
14.15
14.10
14.05
14.00
V/Z (Å3•atom-1)
300
400
500
600
700
800
900
1000
T (K)
hcp-Ir0.55Os0.45
hcp-Os

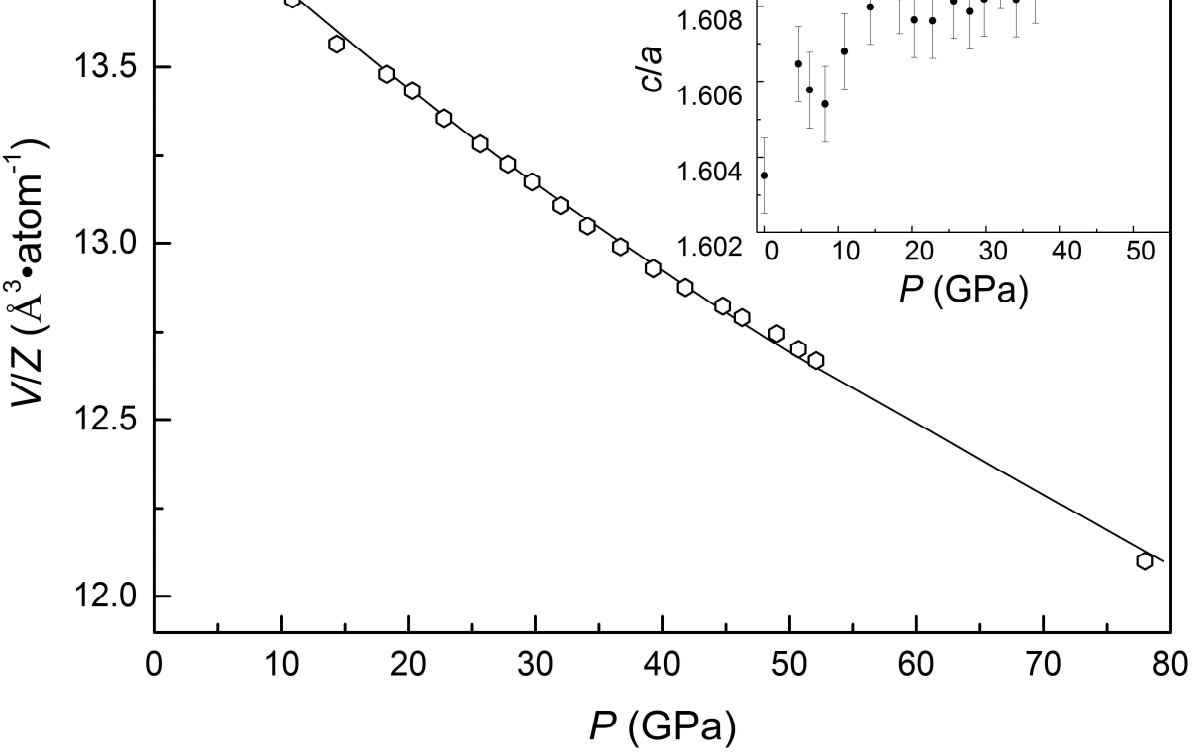

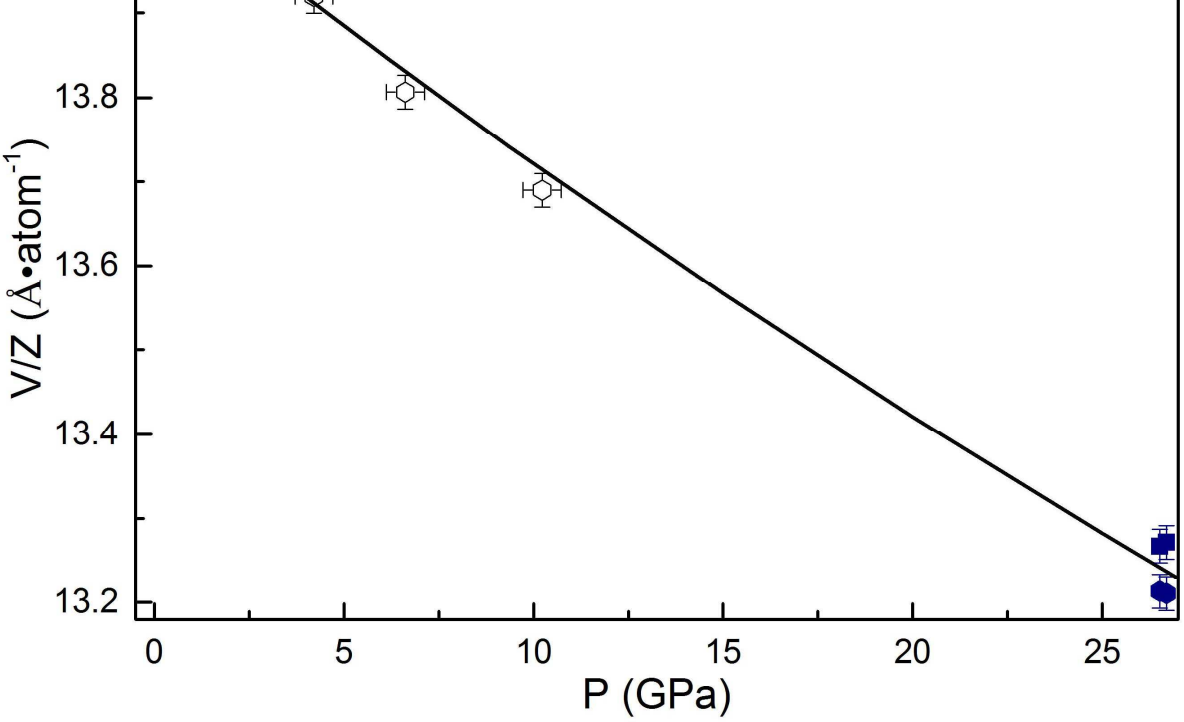

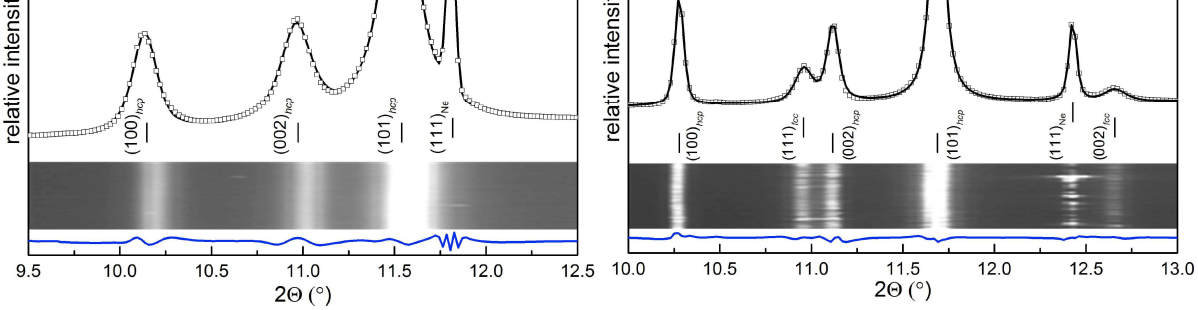

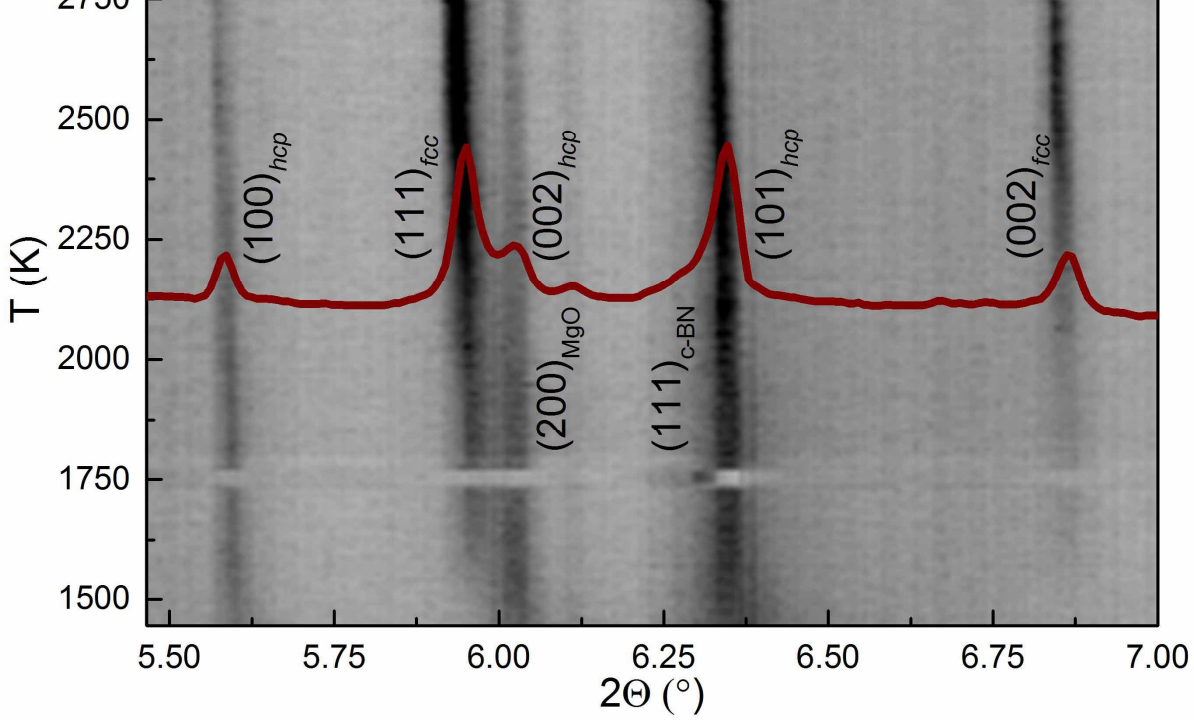
T (K)
2750
2500
2250
2000
1750
1500
5.50
5.75
6.00
6.25
6.50
6.75
7.00
2Θ (°)
(100)hcp
(111)fcc
(002)hcp
(200)MgO
(111)c-BN
(101)hcp
(002)fcc

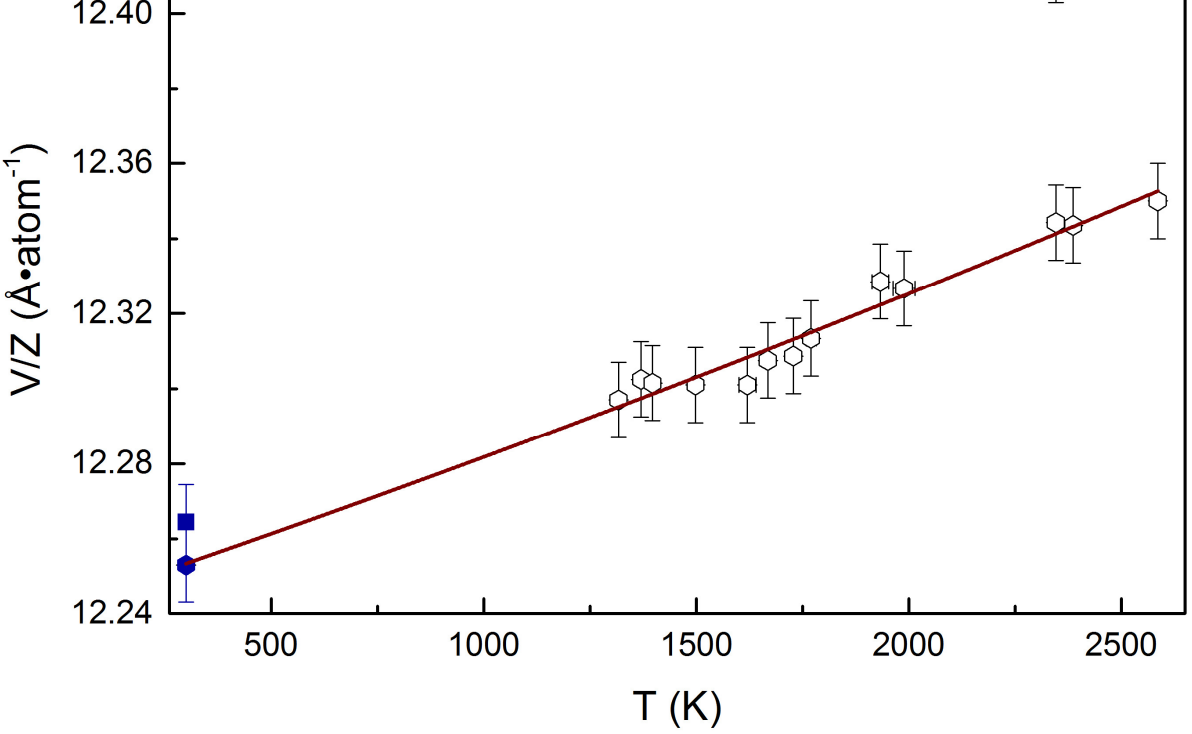

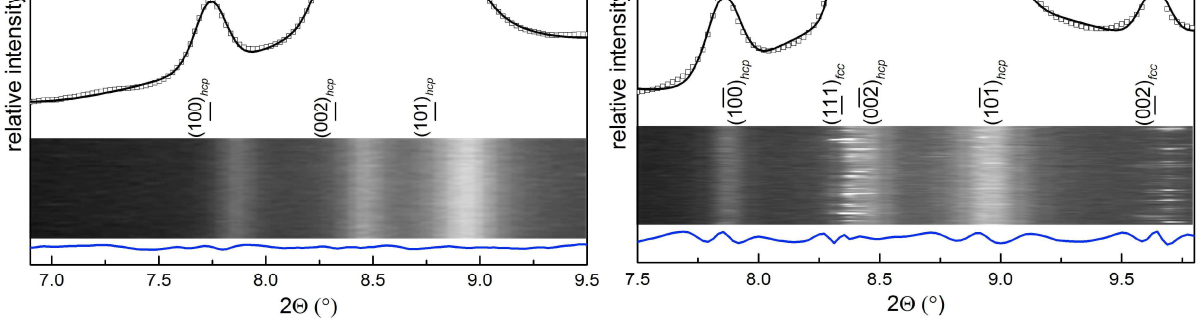

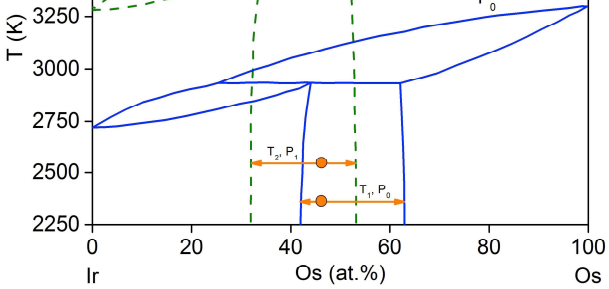

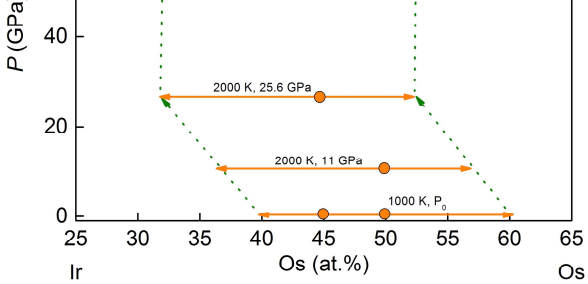

precursors $(NH_4)_2[Ir_xOs_{1-x}Cl_6]$.

A crystalline intermediate has been detected in thermal decomposition of $(NH_4)_2[Ir_xOs_{1-x}Cl_6]$.

Stability of *hcp*-Ir─Os alloys has been tested under high-pressure high-temperature.

Miscibility gap shifts towards iridium with compression.